Theses and Dissertations

Spring 2019

# Flow structures and aerodynamic loads of a rolling wing in a free stream

Randall Berdon
*University of Iowa*

Follow this and additional works at: https://ir.uiowa.edu/etd

Part of the Mechanical Engineering Commons

### Recommended Citation

www.manaraa.com

FLOW STRUCTURES AND AERODYNAMIC LOADS OF A ROLLING WING IN A

FREE STREAM

by

Randall Berdon

A thesis submitted in partial fulfillment of the
requirements for the Master of Science
degree in Mechanical Engineering
in the Graduate College of
The University of Iowa

May 2019

Thesis Supervisor: Associate Professor James H. J. Buchholz

# ACKNOWLEDGEMENTS

I would like to start by thanking Professor James Buchholz for providing the opportunity to further my education as well as the excellent guidance and insight into my experiments, thesis, and scheduling throughout the trying duration of my graduate school career. I could not have made it to this point without him.

I would like to extend my gratitude to the prestigious committee of Dr. H.S. Udaykumar and Dr. Caterina Lamuta for taking the time to review my work as well as present all I have done throughout graduate school.

Kevin Wabick and Austin Krebill, I am honored to have been part of your team and I could not have asked for better lab mates. I would also like to further extend thanks to Kevin for co-collaborating on numerous projects and endeavors throughout my Masters Degree.

Furthermore, I would like to appreciate Mr.Kyle Johnson and Dr. Brian Thurow for the collaboration and giving us the chance to use the amazing plenoptic PIV system.

Finally, I would like to thank my parents for all the support and my upbringing as well as my friends for providing me with all the great memories I will hold on to forever.

# ABSTRACT

The leading-edge vortex (LEV) is a structure found in unsteady aerodynamics that can alter the forces induced on wings and other rotating structures. This thesis presents an experimental study on LEV development on low aspect-ratio wing rolling in a uniform flow at high angles of attack. The flow structure dynamics of rotating wings in the presence of a free stream are not well understood due to the limited studies under these conditions. In this study, a broad parameter space with varying advance ratio and wing radius of gyration are analyzed using dye-visualizations. In most cases, either a conical LEV structure developed on the inboard part of the wing and persisted to a significant roll angle, as well as the arch structure. Plenoptic PIV was used to validate observations in flow visualizations as well as identify finer structures. A binary classification criterion was defined based on the formation and persistence of the inboard conical LEV structure. This criterion identified the LEV as either *conical* ,*non-conical* or *transitional*. Previous studies inspired the proposal of a "rotation parameter" ,$\Pi_{Rot}$, that was a based on a non-dimensional velocity gradient. A value of $\Pi_{Rot} = 0.17$ was found to separate conical and non-conical LEV parameter, suggesting the fundamental importance of this parameter to LEV dynamics. Furthermore, the forces were analyzed to understand the impact of the flow structure on the forces. The conical LEVs had a transient peak followed by irregular udulations while the non-conical LEVs produced high frequency oscillations. In both cases, the force could be understood based on the time-evolution of the LEVs.

Passive bleeding was considered within this study to perturb the flow. Four passive

bleed configurations were experimented with at different hole locations and sizes. It was found that a hole applied near the wing root with a large diameter perturbed the flow and transformed the structure from conical to non-conical classifications. This provides a platform to further understand the flow mechanisms that govern LEV formation and evolution by drastically changing flow structures and maintaining the same geometric and kinematic parameters. Additional studies were done analyzing the changes on the forces on the wing. The lift on the passive bleeding did not seem to be affected however, the thrust was decreased to nearly 0.

# PUBLIC ABSTRACT

In unsteady aerodynamics, the leading-edge vortex (LEV) is a fluid feature that has been found to alter the forces on rotating structures. Currently, the aerodynamics of rotating wings in the presence an approach velocity is not well understood due to limited studies under these conditions. This thesis examines a broad parameter space altering the radius of gyration as well as the rotational velocity using dye-visualizations. Plenoptic Particle Image Velocimetry measurements were performed to validate dye-visualizations. Observations from dye-visualizations were used to create a classification criterion based on the inboard portion of the LEV. The criterion identified the LEVs as *conical* , *transitional*, or *non-conical*. A "rotation" parameter, $\Pi_{Rot}$, based on a non-dimensional velocity gradient along the wing span was proposed and found to separate the classified *conical* and *non-conical* LEVs. Forces were measured on the wing to understand the impact of the flow structures on the aerodynamic loads. Additionally, 4 passive bleeding studies were performed by placing miniature through holes of different diameters and locations to perturb the flow. With passive bleeding applied inboard and the larger hole diameter, transformed the conical LEV to a non-conical LEV despite keeping the kinematics and geometry the same. This is important because it provides a platform to further understand mechanisms that govern the LEV evolution. Finally, the forces were measured for the passive bleeding configuration with the largest impact on the flow structure and was found to alter the drag and not the lift of the wing.

# TABLE OF CONTENTS

# LIST OF TABLES

Table

# LIST OF FIGURES

# CHAPTER 1
# INTRODUCTION

The leading-edge vortex has been found to be a significant feature in the context of maneuvering wings. The leading-edge vortex (LEV) creates a suction as well as other effects that have been found to impact the forces on the wing. Ellington et. al [3] showed the circulation accumulated in the LEV which increases the lift. A deeper understanding for the leading edge vortex (LEV) would be beneficial in rotating helicopter blades, turbines, along with many aircraft and many other aerospace applications.

The flow around airfoils and wings are complicated and have been studied for years. Himmelskamp [6] found that the forces on a propeller blade were altered due to the effects of rotation. Since then, Lentik and Dickinson[4] proposed a theoretical framework from a non-inertial reference frame that expressed the significance of kinematics and morphology. The Navier-Stokes equations were non-dimensionalized from which the angular acceleration number, the centripetal acceleration number, and Rossby number were derived as shown in equation 1.1 - 1.3.

$$\frac{\dot{\Omega}^2 Rc}{U^2} = \frac{1}{C_{ang}} \tag{1.1}$$

$$\frac{\Omega^2 Rc}{U^2} = \frac{1}{C_{cent}} \tag{1.2}$$

$$\frac{\mu}{\rho Uc} = \frac{1}{Re} \tag{1.3}$$

It was demonstrated that by increasing the radius of gyration, the curvature of the path traveled decreases as radius increases. This would imply that at lower radii of gyration the 3D angular acceleration has a far greater impact as opposed to larger radii of gyration for which the wing has a constant velocity distribution in the spanwise direction that is similiar to that of a purely translating wing.

Many studies have been performed for rotating wings in quiescent fluid to isolate the effects of rotation at a canonical level. Wojcik and Buchholz[13] conducted a parametric study varying the angle of attack, local Reynolds number, and aspect ratio . It was highlighted that the increase in angle of attack increased the size of the LEV as well as increased the finer scale structures. Additionally, the tip effects were observed to stabilize the LEV as the wing aspect ratio of two had a much more consistent circulation in comparison to a wing aspect ratio of four. The most significant finding however, for all non-dimensional circulation values defined as $\Gamma^* = |\Gamma_{LEV}| / |\Gamma_{th}|$ collapsed moderately over the Reynolds number and angles of attack. This could have implications that the circulation from the LEV dominates the bound circulation. Wolfinger and Rockwell[14] subsequently, aimed to better understand the significance of the radius of gyration in rotating wings. Experiments were performed in quiescent fluid with an aspect ratio 2 wing. The velocity at the radius of gyration remained constant across all experimental cases with $V_{rg}$ = 49 mm/s. Radii of gyration $R_g/c$ = 1.7 and 4.7 were investigated. Iso-surface of Q were plotted for $Rg/c$ = 1.7 and 4.7 and it was observed that at the lower radii of gyration a coherent conical vortex formed and persisted throughout the maximum distance of travel. Conversely, at $R_g/c$ = 4.7, an arch structure forms and convects downstream during the duration of the

motion. Similarly, Jones and Babinsky [9] performed a study in quiescent fluid however, unsteady flow fields were captured via the towing and pivoting of a wing with an aspect ratio of 4. In this study it was found that the circulation on a wing increases until the point of max lift. After this point the LEV was found to pinch off and convect downstream. This is in support of the argument that the LEV increases the overall lift on a wing.

Bross et. al[2] investigated the impact of advance ratio $J = U_\infty/U_{tip}$ for a rolling wing advancing in a uniform flow, where $U_\infty$ is the velocity of the free stream, and $U_{tip}$ is the velocity of the wing tip due to rotation. Reynolds number with the use of the effective tip velocity ($U_{eff} = \sqrt{U_\infty^2 + U_{tip}}$) of Re = 23430,10766, 11257, and 12030 corresponding to J =0, .179,.358, and .537 respectively. A stable LEV was observed for the extremes (i.e. J=0 and .537) up to a rotation angle Φ=36 degrees. Experiments showed that the LEV development was fairly consistent across the range of J values at an $R_g$/c = 1.85.

To develop further insight into the mechanisms by which wing rotation governs the vortex dynamics in rotating flows, Jardin and David [7] conducted simulations to compare the flow evolution on a rectangular wing of aspect ratio 4 in a uniform approach flow, a shear flow representing the spanwise gradient of velocity experienced by a rotating wing in quiescent flow, and a rotating wing in quiescent flow. They found qualitatively and quantitatively the effect of an incoming shear flow on a wing. An aspect ratio 4 wing maintaining a $\alpha_{eff} = 45°$ was used for investigation of a wing in uniform flow, a wing in shear incoming flow, and a purely revolving wing in quiescent fluid. The wing in the uniform flow exhibited significantly different flow characteristics as the LEV in this case shed. It was however, observed through iso-surfaces that the wing in shear flow and the purely revolving wing had

similar flow evolution and structures. In both cases the wing generates an LEV that remains attached except near the vicinity of the tip. This demonstrates, clearly, the shear velocity gradient has an impact in the context of rotating wing and could potentially be the governing mechanism of rolling wings.

Currently, the vortex dynamics of a rolling wing in the presence of a free-stream is not well-understood due to the lack of studies that have been performed. In this paper, a broad parameter space will be explored varying $J$ and $R_g/c$ through flow visualizations. Finer structures and validation of flow visualization through plenoptic PIV is also performed. Furthermore, the exploration of a similarity parameter based on a non-dimensional velocity gradient is conducted. Finally, the flow is perturbed through passive bleeding to provide an even deeper understanding to the governing mechanisms for LEV growth and evolution while providing a platform for future analysis.

# CHAPTER 2
# METHODOLOGY

## 2.1 Overview

In this study, a rectangular-plate of aspect ratio 2 performed an initial roll maneuver in the presence of a uniform free stream while maintaining a constant angle of attack. The free stream velocity produced a chord based Reynolds number of 10000. Dye visualizations were performed across 4 radii of gyration and 6 advance ratios. Plenoptic PIV data was subsequently obtained for 2 cases to validate flow visualizations as well as capture finer details of the flow. Force measurements were acquired for four different cases in the absence of passive bleeding to relate the flow structures to the forces on the wing. Finally, one of the cases was repeated with a modified wing with a hole near the root, creativity a passive bleed perturbation significantly altering the flow. Four different configurations of passive bleed were investigated, and one cases was selected for further investigation using force measurements. A force analysis of the baseline vs the passive bleeding case was conducted to understand the impact of changing the flow structure while still maintaining the same kinematics and geometry.

## 2.2 Experimental Setup

A flat-plate wing of aspect ratio 2 was manufactured from clear colorless acrylic to minimize laser reflections, and had a chord length, $c = 76.3$ mm , span $b = 152.6$ mm, and thickness of 3.3% of the chord, with both the leading and trailing edges rounded with a constant radius of half the plate thickness to eliminate separation caused by edges. To

ensure negligible deflection, the root of the wing was inserted into a bracket extending the full chord length, and supported by a 3.2 mm diameter rod at the leading edge. Plate features and dimensions are presented in figure 2.1.

Figure 2.2 illustrates the motion mechanism and wing. The wing was articulated in a roll maneuver about an axis aligned with the free stream, and coincident with the surface of a skim plate extending approximately 0.45 m upstream and 0.78 m downstream of the wing mid-chord. The motion was achieved using an Emerson XVM-8020-TONS-000 DC servo motor driven by an Emerson EP-204B servo drive and Galil DMC-4040 motion controller. A second servo motor was used to maintain static pitch angles during experiments. Experiments were conducted in the University of Iowa's free-surface water channel with test section width of 0.61 m, and water depth of 0.33 m. The water channel has flow conditioning consisting of an 8:1 contraction ratio, honeycomb, and five screens to maintain free stream turbulence intensity below 0.3%.

### 2.3   Parameters

A wing Reynolds number of 10,000 was maintained, based on the free-stream velocity, $U_\infty$ and chord length of the wing, $c$:

$$Re_c = \frac{U_\infty c}{\nu} \tag{2.1}$$

where $\nu$ is the kinematic viscosity of the water. Additionally, the effective angle which is defined defined the radius of gyration, $R_g$, remained at a constant $\alpha_{eff} = 33°$. The effective angle of attack is dependent on the geometric pitch angle $\alpha_{geo}$ and the advance
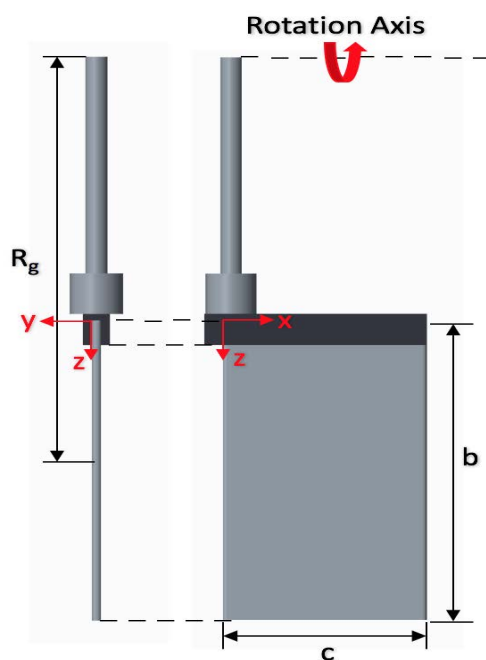
Figure 2.1: Plate geometry
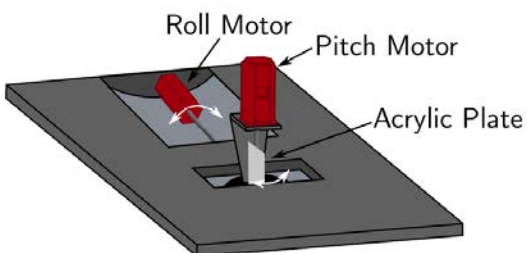


Figure 2.2: Experimental set-up for the pitching and rolling flat plate
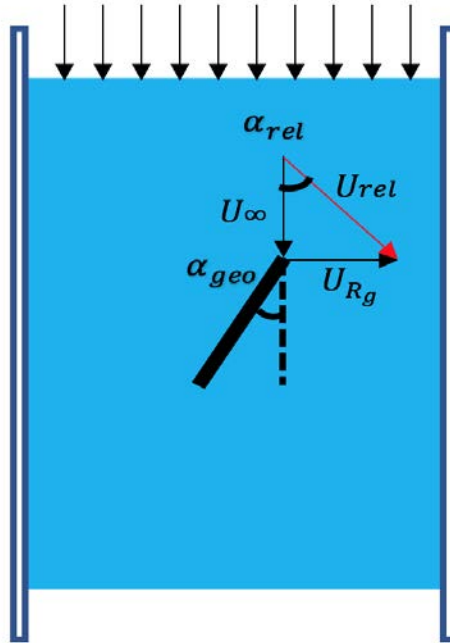
Figure 2.3: Demonstration of the $\alpha_{eff}$

ratio, J of the wing:

$$\alpha_{eff} = \alpha_{geo} + \arctan\frac{1}{J} \tag{2.2}$$

An important velocity scale is the relative velocity magnitude, $U_{rel}$, which results from the vector addition of the rolling velocity at the radius of gyration and the free stream velocity. A constant effective angle of attack $\alpha_{eff} = 33°$. The advance ratio ratio is a parameter is known to be relevant in the context of rotational blades. The advance ratio $J$ is the ratio between the free stream velocity $U_\infty$, and the rotational velocity at some radius away from the axis of rotation $U_R$ (i.e. equation 2.3).

$$J = \frac{U_\infty}{U_{R_g}} \tag{2.3}$$

$$U_R = \Omega_x R \tag{2.4}$$

For the cases considered within this study, the rotational velocity used to calculate $J$ was considered at the radius of gyration and referred to as $U_{R_g}$:

$$U_{R_g} = \Omega_x R_g \tag{2.5}$$

With $\Omega_x$ being the rotation rate in $rad/s$. The approach velocity at the leading-edge of the wing $U_{rel}$, is found by considering the combination of the both the magnitude and direction of $U_\infty$ and $U_{R_g}$. To calculate the relative velocity, the RMS of $U_\infty$ and $U_{R_g}$ was taken:

$$U_{rel} = ((U_{R_g})^2 + U_\infty^2)^{\frac{1}{2}} \tag{2.6}$$

Another parameter that has been found to be relevant in the context of rotation is the radius of gyraton $R_g$. The radius of gyration can be non-dimensionalized by an array of different reference length however, in this case, the radius of gyration is non-dimensionalized by the chord which has been a common practice in the context of rotating wings. The radius of gyration is defined as the square root of the ratio between the modified moment of inertia, $I_x'$, and the area of the rectangular plate, $A$:

$$R_g = \sqrt{\frac{I_x'}{A}} \tag{2.7}$$

$$A = b * c \tag{2.8}$$

where the modified moment of inertia is considered from the centroid of the plate to the axis of rotation. This has implications that the parallel axis theorem is used for the modified moment of inertia:

$$I_x' = I_x + Ad^2 \tag{2.9}$$

where $d$ is the distance from the axis of rotation to the centroid of the rectangular plate.

The dye visualizations were done over a wide spread array of different values to broaden the understanding and behavior of the LEV. Combinations of 6 different $J$ values and 4 different non-dimensional radii of gyration $R_g/c$ were used. Values included $J = 0.325, 0.542, 0.813, 1.08, 1.36$, and $1.54$ along with $R_g/c = 2, 2.5, 3.25$, and $3.5$. A summary of all the flow visualization cases that are used in the absence of passive bleed are provided in 2.1. In this paper, the following nomenclature will be used to define different roll cases $R_J^{R_g/c}$. The R stands for pure roll while the subscript is the advance ratio and the superscript is the non-dimensional radius of gyration.

The total set of plenoptic data included purely pitching cases, purely rolling cases, and simultaneous pitching and rolling cases. This paper focuses on the $J = 0.54$ and $1.36$
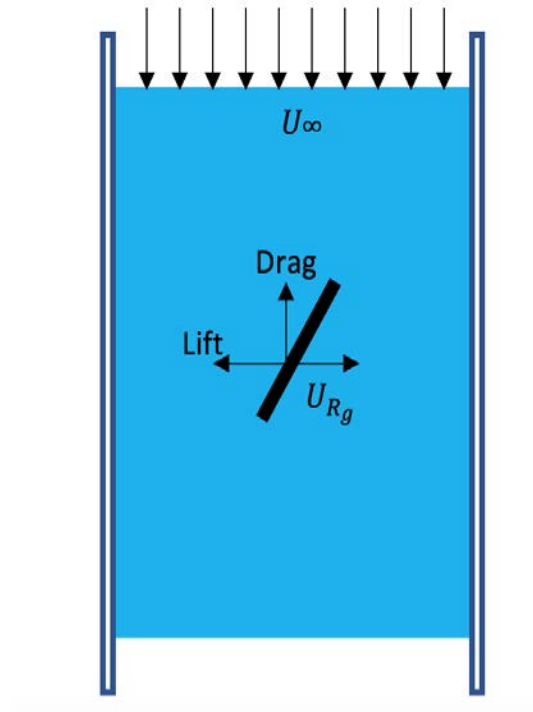
Figure 2.4: Lift and drag force directions

at a $R_g/c = 3.25$ to validate flow visualizations. Passive bleed was conducted on the $R_{0.54}^{3.25}$ case.

Force measurements were also conducted over the advance ratios $J = 0.54$ and $1.36$ with $R_g/c = 2.5$ and $3.25$. The direction of the lift was defined as perpendicular to the free stream while drag was parallel to the free stream as shown in figure 2.4.

A common practice in the aerospace industry is to non-dimensionalize the force coefficients by $U_\infty$:

$$C_L = \frac{2L}{\rho U_\infty^2 bc} \tag{2.10}$$

$$C_D = \frac{2D}{\rho U_\infty^2 bc} \tag{2.11}$$

where $L$ and $D$ are the lift and drag forces respectively. In this equation, $\rho$ is the density of the water. For this study, the force coefficients were also non-dimensionalized by the relative velocity $U_{rel}$:

$$C_L = \frac{2L}{\rho U_{rel}^2 bc} \tag{2.12}$$

$$C_D = \frac{2D}{\rho U_{rel}^2 bc} \tag{2.13}$$

Non-dimensionalizing by $U_{rel}$ is advantageous because this parameter isolates the forces imposed by the flow structure.

Passive bleeding was applied in this study to alter the flow structure in hopes to further understand the mechanisms that govern the LEV evolution and behavior. Passive bleeding in this case was applied by adding a through hole to the wing at different locations. The $R_{0.54}^{3.25}$ were used as the baseline case because a conical structure was observed and re-mained attached throughout the motion. Through holes were added at 2 different locations and hole sizes. It is important to note that for all of the studies, only a single through hole was open at each instance. A diagram of the through hole locations are shown in figure 2.5.

Passive bleeding visualizations were recorded at constant values of $J = 0.54$, $R_g/c = 3.25$, $\alpha_{eff} = 33°$, and maximum roll angle $\phi = 60°$. The five different Passive Bleeding cases are shown in Table 2.2. The naming convention for the passive bleeding cases will be $p_{xy}$ where x is the spanwise location as indicated in the prior section by $i$ or $o$

| Case | $\alpha_{eff}$ | $\alpha_{gem}$ | $R_g/c$ | J | Cases |
|---|---|---|---|---|---|
| $R_{0.54}^{2.00}$ | 33° | -28.3° | 2 | 0.54 | X |
| $R_{0.81}^{2.00}$ | 33° | -17.9° | 2 | 0.81 | X |
| $R_{1.08}^{2.00}$ | 33° | -9.8° | 2 | 1.08 | X |
| $R_{1.36}^{2.00}$ | 33° | -3.3° | 2 | 1.36 | X |
| $R_{1.56}^{2.00}$ | 33° | 0.3° | 2 | 1.56 | X |
| $R_{0.33}^{2.50}$ | 33° | -39.0° | 2.5 | 0.33 | X |
| $R_{0.54}^{2.50}$ | 33° | -28.3° | 2.5 | 0.54 | X |
| $R_{0.81}^{2.50}$ | 33° | -17.9° | 2.5 | 0.81 | X |
| $R_{1.08}^{2.50}$ | 33° | -9.8° | 2.5 | 1.08 | X |
| $R_{1.36}^{2.50}$ | 33° | -3.3° | 2.5 | 1.36 | X |
| $R_{1.56}^{2.50}$ | 33° | 0.3° | 2.5 | 1.56 | X |
| $R_{0.54}^{3.25}$ | 33° | -28.3° | 3.25 | 0.54 | X 0 |
| $R_{1.36}^{3.25}$ | 33° | -3.3° | 3.25 | 1.36 | X 0 |
| $R_{0.33}^{3.50}$ | 33° | -39.0° | 3.5 | 0.33 | X |
| $R_{0.54}^{3.50}$ | 33° | -28.3° | 3.5 | 0.54 | X |
| $R_{0.81}^{3.50}$ | 33° | -17.9° | 3.5 | 0.81 | X |
| $R_{1.08}^{3.50}$ | 33° | -9.8° | 3.5 | 1.08 | X |
| $R_{1.36}^{3.50}$ | 33° | -3.3° | 3.5 | 1.36 | X |
| $R_{1.56}^{3.50}$ | 33° | 0.3° | 3.5 | 1.56 | X |

**X = Flow Visualization   0 = Plenoptic PIV**   [blue box] **= Force Measurements**
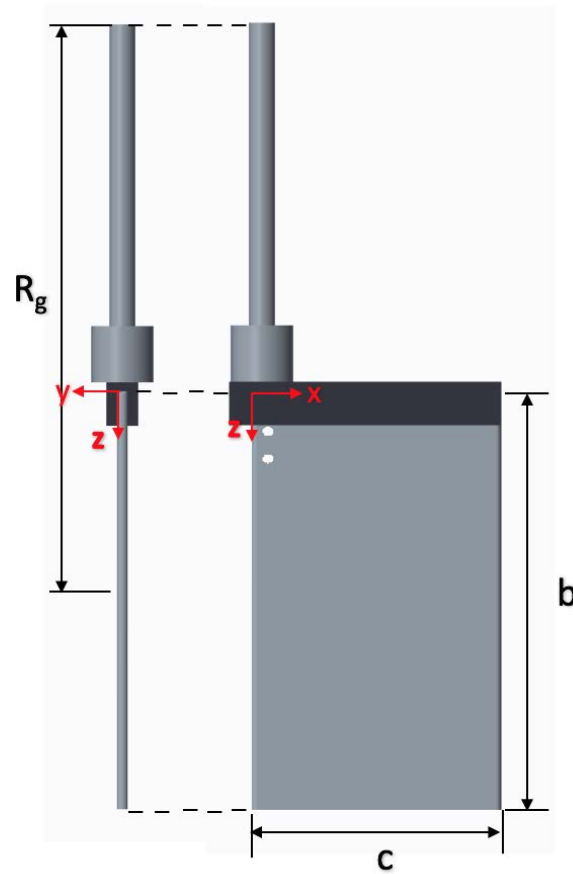
Table 2.1: Flow Visualization Parameter Space

Figure 2.5: Passive bleed hole locations

| Name | Advance Ratio (J) | Hole Spanwise Location ($z/b$) | Hole Chordwise Location ($x/c$) | Hole Diameter (mm) | Cases |
|---|---|---|---|---|---|
| Baseline | 0.54 | N/A | N/A | N/A | X |
| $p_{is}$ | 0.54 | 0.1 | 0.065 | 1.6 | X |
| $P_{os}$ | 0.54 | 0.16 | 0.065 | 1.6 | X |
| $p_{il}$ | 0.54 | 0.1 | 0.065 | 3.2 | X |
| $P_{ol}$ | 0.54 | 0.16 | 0.065 | 3.2 | X |

X = Flow Visualization ▭ = Force Measurement

Table 2.2: Passive Bleed Hole Locations

and y is the hole size designated by *s* or *l*. Passive bleeding was applied for singular holes at each instance.

Force measurements were later conducted with $J = 0.54$ and $R_g/c = 3.25$ in the absence of bleed and then with $P_{il}$ case because drastic flow changes were observed. This comparison was useful for identifying the impact of changing the flow structure while keeping the same kinematics and geometry.

## 2.4 Dye Visualization

For flow visualizations, a mixture of Elmer's water soluble glue and fluorescein disodium salt was mixed. The dye-glue mixture was applied in an approximately 0.5 cm strip at the leading-edge. Videos were recorded with a Nikkon D3100 camera with a 105 mm Nikkon f/28 macro-lens. An fstop of f/8 was used with an ISO of 3200. The shutter speed was set to 1/80 s. A summary of the parameter space is shown in table 2.1 and 2.2.
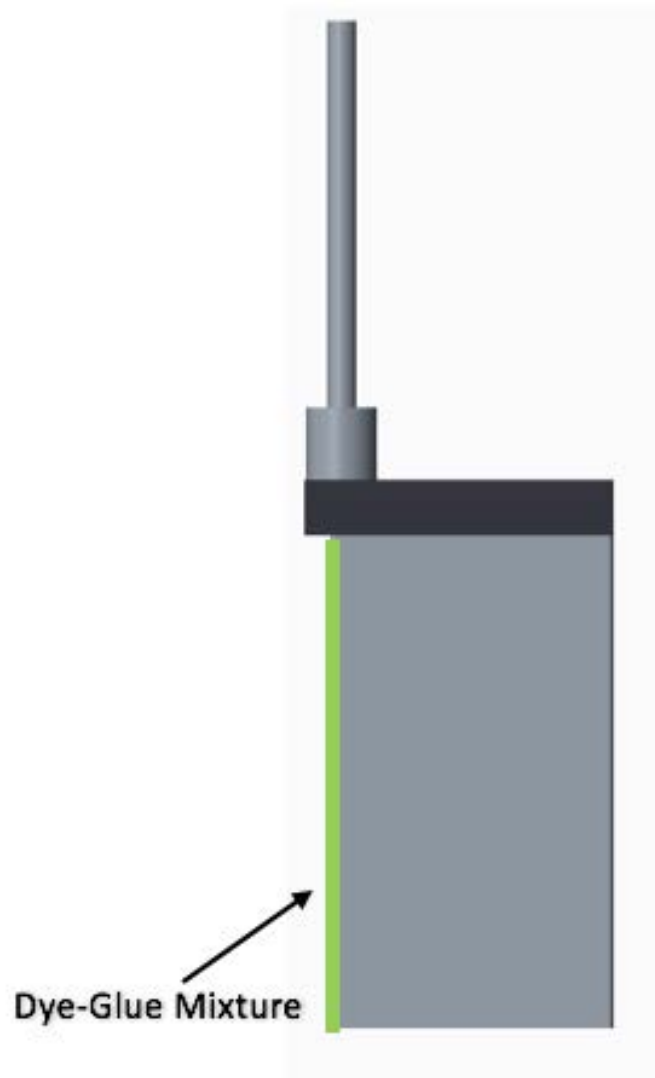
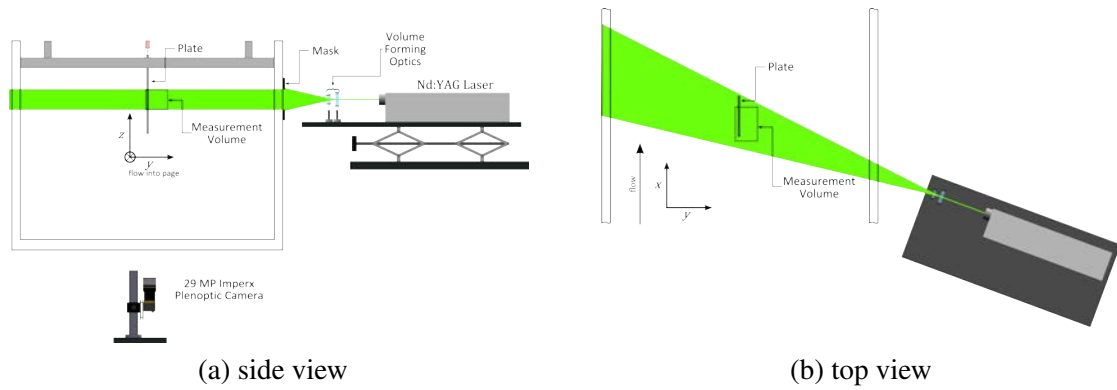Figure 2.6: Application of the dye visualization

(a) side view                                    (b) top view

Figure 2.7: Experimental arrangment from Johnson et. al [8]

## 2.5    Plenoptic PIV

3-D plenoptic measurements were captured in collaboration with Mr.Kyle John-son and Dr.Brian Thurow using a microlens array designed by Aurburn University. The benefit in using the plenoptic setup is that the camera can reconstruct volumes by capturing both spatial and angular information. The multiplicative algebraic reconstruction technique (MART) was used to reconstruct volumes using the plenoptic images. Fahringer et al.[5] provides a clear description and demonstration of the MART technique. The ensemble-averages were computed at different $\phi$ during the motion. The modified 29 megapixel Imperx Bobcat B6620 camera was setup below the flume while a 200 mJ/pulse dual-cavity Nd:YAG laser illuminated the volume from the side of the flume. The volume was created by masking the laser at the side of the flume in the z direction. A 102 mm $\times$ 68 mm $\times$ 68 mm volume was captured during the study. The configuration is shown in figure 2.7. A sample of raw images are shown in 2.8.

Reflections were removed using the proper decomposition method (POD) following
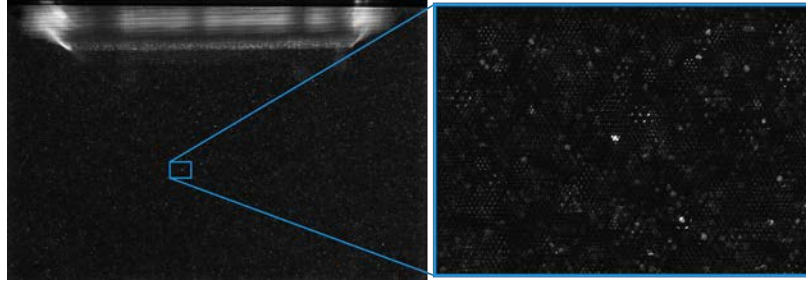
Figure 2.8: A raw plenoptic particle image produced by Johson et. al [8]

similar to guidelines highlighted by Mendez et. al [11]. Ultimately, the 20 most energetic modes were subtracted from each mode. Subsequently, 3 iterations of MART and a relaxation parameter $\mu = 1.0$ particle volumes were reconstructed onto a discretized grid of 527 voxels $\times$ 357 voxels $\times$ 357 voxels. The final correlation volume had a 3.3 mm $\times$ 3.2 mm $\times$ 3.2 mm which corresponds to a vector spacing of 1.6 mm in all directions. Alignment was done manually by selecting image pairs to accurately align the data.

Mr. Kyle Johnson produced contours of normalized swirling strength as defined in equation 2.14 .

$$\hat{\lambda}_{ci} = \frac{\lambda_{ci}^2}{max\lambda_{ci}^2} \tag{2.14}$$

The swirling strength was calculated using the $\lambda_{ci}$ criterion identified by Zhou et. al [16]. In the $\lambda_{ci}$ criterion, the vortex is identified using the imaginary portion of the complex eigenvalues of the velocity gradient tensor. This quantity eliminates areas such as shear layers where vorticity is present but a swirling motion is not. Contours were created at 0.1 and 0.25 with stream ribbons that was colored by chordwise velocity, $U'$.

## 2.6  Force Measurements

Force measurements were conducted globally for the wing with a 6 axis ATI Mini-40. The force transducer was attached in between the pitch motor and the extension rod attached to the wing as shown in figure. Whereas measurements of the hydrodynamic loading on the wing were desired, the measured forces included the buoynacy, static, gravitational, and wing inertial forces. Isolation of the hydrodynamic forces required multiple different experiences. The rolling wing in water had buoyancy, static, gravitational, and inertial forces while the wing in air included only inertial and gravitational forces. Forces were also recorded on the wing at roll angles of 5° increments ranging from $\phi = 0°$ to 60°. The static cases in air had gravitational forces, while the static cases in water have buoyancy and gravitational forces.The hydrodynamic forces were extracted from the gravitational, buoyancy, inertial, static, ahd hydrodynamic forces which are the $F_G, F_B, F_I, F_S$, and $F_H$ respectively. The full measurements in water $F_{full}$, and air $F_{air}$ and the static measurements in water $F_{(static, water)}$ and air $F_{(static, air)}$.

$$F_H = F_{full} - F_{air} - F_{static,water} - F_{static,air} \tag{2.15}$$

$$F_H = (F_H + F_G + F_I + F_B) - (F_I + F_G) - (F_G + F_B) - (F_G) \tag{2.16}$$

# CHAPTER 3
# FLOW STRUCTURE AND FORCES

Figure 3.3, 3.4, and 3.5 contains example dye visualizations illustrating the variation in flow structures with changes in $R_g/c$ and $J$. The variation of the non-dimensional radius of gyration $R_g/c$ and the advance ratio $J$ within the investigated parameter range revealed variation in LEV behavior in an apparent continuum of states between a well-defined conical structure bound near the leading edge of the wing, and an arch structure pinned to the wing only at the tip and root Visbal et. al [12]. To assess the effect of wing rotation, parameterized through $R_g/c$ and $J$, the LEV structure was qualitatively categorized based on an objective characterization intended to identify whether the dominant behavior of the LEV was primarily conical or non-conical. Plenoptic PIV data was taken to validate what is seen in flow visualization as well as resolve finer structures that cannot be seen in flow visualizations. The force coefficients on the wing are measured and analyzed to further understand the impact of changes in the flow.

## 3.1 Qualitative Characterization Of LEV Development Using Flow Visualization

Figure 3.1 a and b demonstrate flow visualizations of $R_{0.54}^{3.25}$ and $R_{1.36}^{3.25}$ cases respectively. In each of these cases the LEV forms and behaves significantly different, and were useful in identifying the distinct flow structures which are used to define a classification criterion for LEV behavior for rolling wings. The $R_{0.54}^{3.25}$ maintains a relatively symmetric LEV in spanwise direction till at least $\phi = 16°$. A significant and energetic tip vortex has developed across the the entirety of the chord and continues into the wake. As the motion
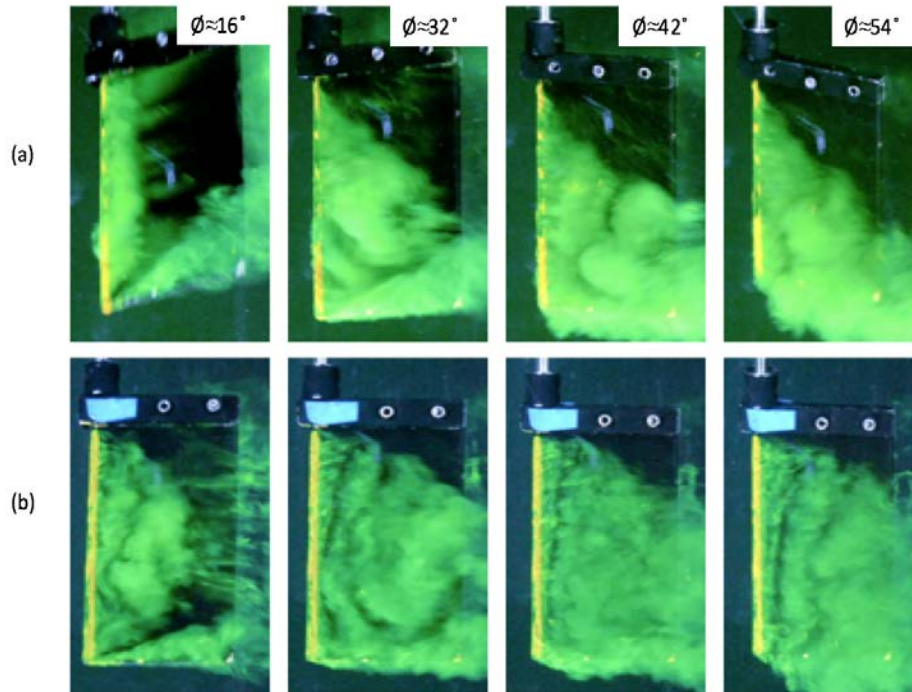
Figure 3.1: LEV evolution for (a) $R_{0.54}^{3.25}$, $\alpha_{eff} = 33°$ (b) $R_{1.36}^{3.25}$, $\alpha_{eff} = 33°$

continues, by $\phi = 32°$, the inboard conical region has developed to about the 60% spanwise position. In the outboard region, an arch structure has formed. The tip vortex persists and remains coherent as well as highly energetic. By $\phi = 42°$ the arch structure has shed and 2 discrete structures are present in the outboard region. At the inboard region, the LEV maintains the conical shape and remains coherent. In the tip region, the tip vortex has interacted with the LEV and is no longer tight and energetic. This region is highly three-dimensional and chaotic. At $\phi = 54°$, the inboard region continues to maintain the conical structure while the outboard region remains highly three-dimensional.

The $R_{1.36}^{3.25}$ case flow evolves much differently than the $R_{0.54}^{3.25}$ case. The LEV for the $R_{1.36}^{3.25}$ case has rolled up by $\phi = 16°$ and remains pinned at the outboard and inboard edges of the span. A large arch structure has formed near the midspan of the wing and the LEV is fairly symmetric in the spanwise direction. Similar to the $R_{0.54}^{3.25}$ case, an energetic tip vortex has formed. By $\phi = 32°$, the initial LEV has shed along with a secondary LEV that has shed and formed. A third LEV has formed and is still attached. Contrary to the $R_{0.54}^{3.25}$ case, both the shed LEVs and attached LEV remain symmetric in the spanwise direction. In the tip region a tip vortex appears to still be present however it is less coherent. The $R_{1.36}^{3.25}$ case has only 2 regions which include the LEV the spans majority of the wing and the tip region which includes the tip vortex. At $\phi = 42°$, it appears that there is a continuous layer rather than discrete vortices. In the tip region there is no longer a tip vortex present. By $\phi = 54°$ discrete shedding LEVs are present with an LEV attached to the leading edge. The tip vortex remains absent from the wing.

$$R_{0.54}^{3.25} \qquad\qquad R_{1.36}^{3.25}$$

$\phi = 17°$

$\phi = 30°$

$\phi = 40°$

$\phi = 49°$

$$\frac{\lambda_{ci}^2}{\max\lambda_{ci}^2} \quad 0.10 \quad 0.25 \qquad U' \quad -1 \quad 0 \quad 2$$
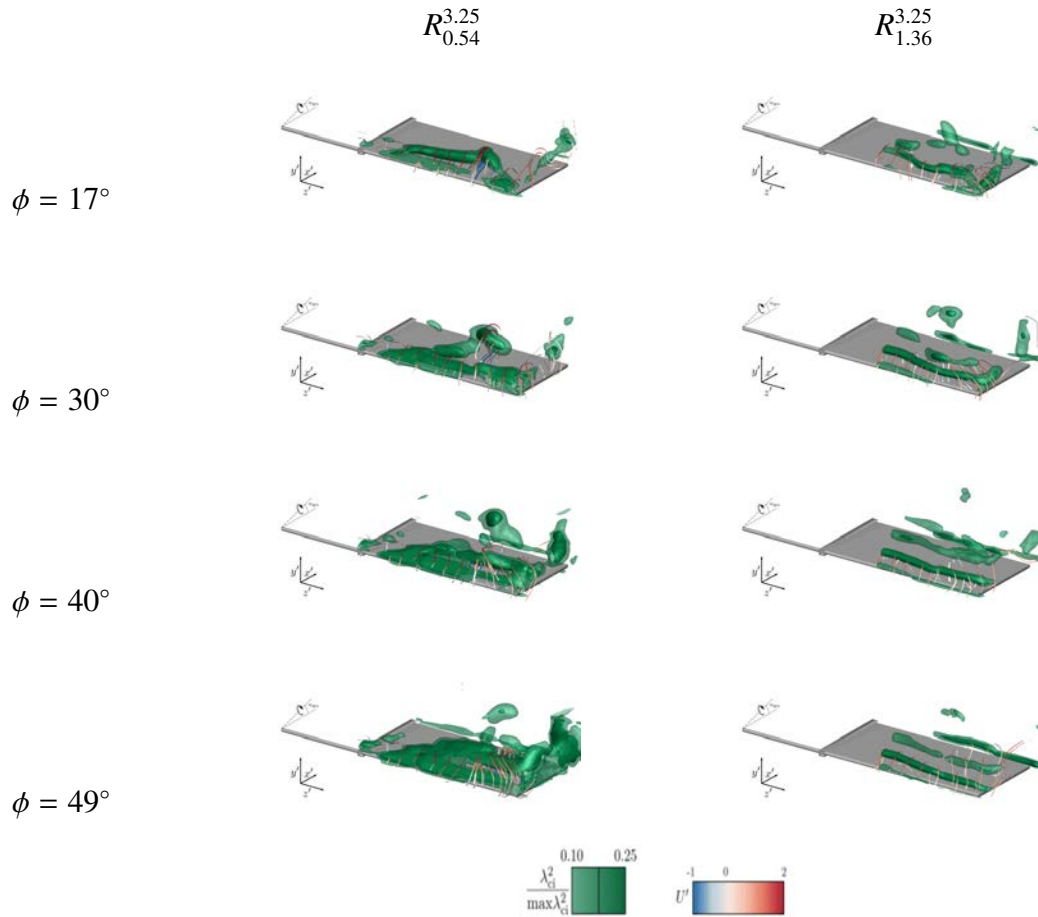
Figure 3.2: Contours of swirl strength for $R_{0.54}^{3.25}$ and $R_{1.36}^{3.25}$ (a)$\phi = 17°$ (b)$\phi = 30°$ (d) $\phi = 40°$ (e)$\phi = 49°$ by Johnson et. al [8]

## 3.2    Plenoptic PIV Analysis

Figure 3.2 shows contours of swirl strength for $R_{0.54}^{3.25}$ and $R_{1.36}^{3.25}$ cases. In the aerodynamic field, swirl strength isocontours are a popular way to identify vortices. These isocontours not only validate the flow visualizations that were discussed in the prior section but also provide a more detailed representation of the flow. Due to the resolution of

roll angles captured using plenoptic PIV, the exact angles shown in figure 3.1 could not be directly compared to plenoptic PIV data. Instead, the closest captured angles during plenoptic PIV are presented for discussion and in figure 3.2. Plenoptic PIV is presented at $\phi = 17°, 30°, 40°$, and $49°$ and compared to the flow visualizations mentioned in the prior sections. At $\phi = 17°$, the $R_{0.54}^{3.25}$ case is similar to the visualization at $\phi = 16°$ in figure 3.1. In both cases, the conical structure is not observed inboard. In the outboard region near the tip, a small arch structure has formed along with the presence of a tip vortex. By $\phi = 30°$, the arch structure that formed near the tip is no longer pinned to the tip region. This can also be seen in the flow visualization at $\phi = 32°$ however, it is harder to identify. In the perspective of which the video was recorded along with how the dye interacts with the vorticity.In both the flow visualization and the plenoptic PIV data, a conical structure is observed at the inboard region of the LEV that persists through entirety of the motion. As the motion continues, the arch structure that was observed in the outboard region has shed by $\phi = 40°$. This forms a large structure along with many discrete structures that is shown in the plenoptic PIV. The large discrete structure appears in the flow visualization shown at $\phi = 42°$ however, visualizations are not able to resolve the finer structures in the flow. Near the surface in the tip region there is a dual vortex structure as seen by Rockwell et. al [15] along with the presence of a tip vortex. The dual vortex structure is not visible in the flow visualization and the tip vortex contains a much different shape than what is observed in the plenoptic isosurface. These observations are a direct result of the limitations of using dye to visualize the flow along with the camera angle that was used to record dye visualizations. The flow is highly chaotic in the tip region at $\phi = 49°$. The dual-vortex structure remains

persists however, at the tip region a disorganized structure is observed. Discrete structures are also present in the region where a large shed discrete structure was observed at $\phi = 40°$. The flow visualizations at $\phi = 54°$ appear to reveal the dual vortex structure however, it is not easily identifiable. The tip region is highly three-dimensional at it is difficult to discern from the dye-visualizations.

For the $R^{3.25}_{1.36}$ case, the flow contains a single LEV that is not attached to the edge along with discrete structures throughout the plate at $\phi = 17°$. A small tip vortex that spans about a quarter of the chord is present. The flow visualizations at $\phi = 16°$, LEV seen in the plenoptic data is present however, the flow visualization appears to have 2 large LEV structures. This is most likely a product of the dye getting entrained by the LEV along with the large structure near the center of the plate. As the motion continues, LEVs shed at a high frequency as new LEVs have both formed and shed at each of $\phi = 30°, 40°$, and $49°$. These observation are also visible in flow visualizations at $\phi = 32°, 42°$, and $54°$ however these vortices appear to have an appearance resembling that of a hemholtz instability due to the rapid shedding of vortices from the leading-edge.

### 3.3 Classification Of The LEV

To objectively characterize the structure of the LEV by varying $J$ and $R_g/c$, a binary classification was established which identified the LEV as *conical* or *non-conical*. The *conical* vortex classification includes a conical-shaped LEV initiating at the root of the wing, remaining coherent for at least 40% of the wing span, and persisting for a sweep angle of at least $\phi= 40°$.The *non-conical* classification includes any cases that do not conform to
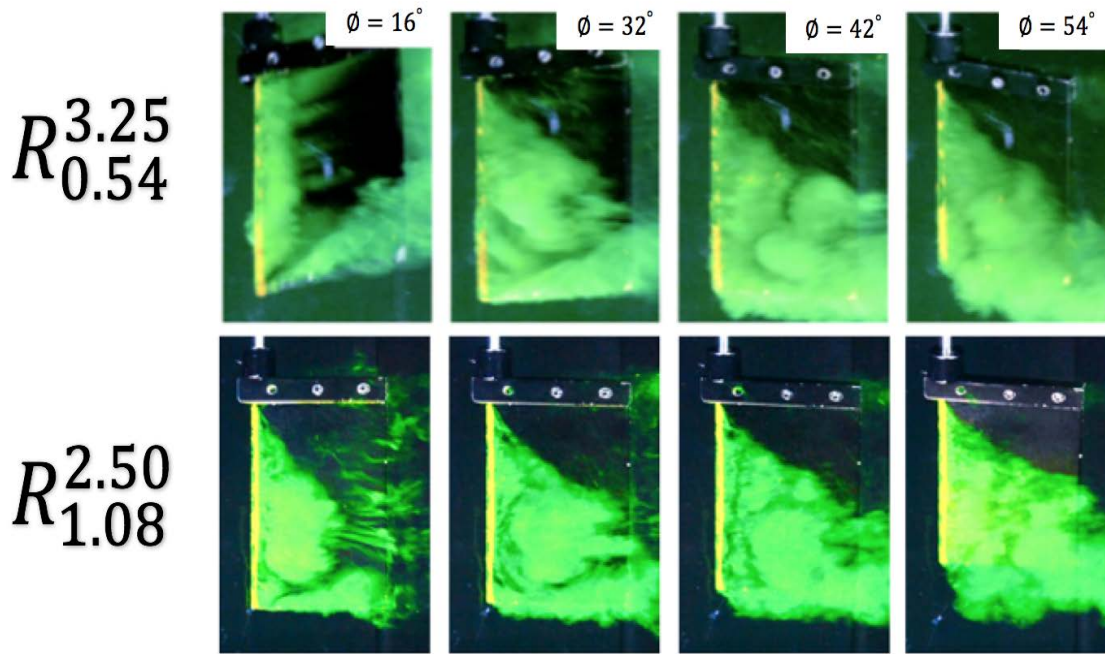
Figure 3.3: Evolution of a *conical* LEV

the *conical* case, and typically includes arch-type LEV structures, as well as the shedding

of multiple LEVs at a much higher frequency than that of the *conical* LEV.

The $R^{3.25}_{0.54}$ and $R^{2.50}_{1.08}$ cases shown in figure 3.3 are examples of *conical* LEVs. The

$R^{3.25}_{0.54}$ case is an example of the most extreme *conical* classification. For this case, the LEV

initially starts off symmetric in the spanwise direction. Subsequently, a distinct conical

structure forms that spans approximately 60% of the total wing span and persists until an

angle of rotation of $\phi = 45°$. Outboard, the dye patterns loses coherence due to the high

3-dimensionality and interactions between the LEV and the tip vortex. The $R^{2.50}_{1.08}$ case is

marginally classified as *conical*. This case follows a similar evolution to the $R^{3.25}_{0.54}$ case with

the distinct difference being an arch structure appears to form outboard and is followed by
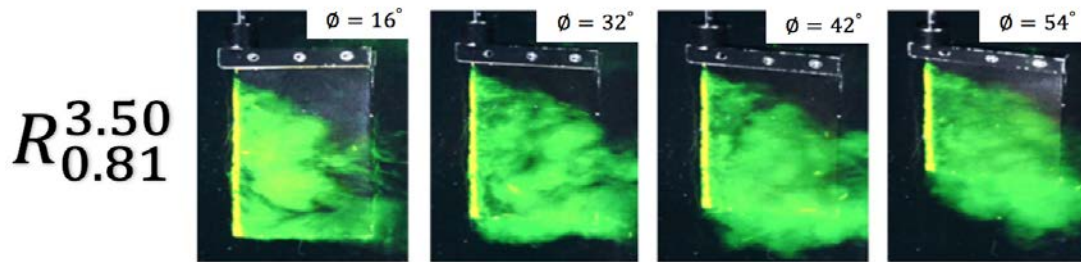
Figure 3.4: Evolution of a *transitional* LEV

the shedding of multiple LEVs. The coherent conical LEV occupies only approximately 40% of the span.

Figure 3.4 shows a *transitional* LEV structure and corresponds to $R^{2.50}_{1.56}$. A *transitional* structure lies in between a *conical* and *non-conical* classification and is difficult to classify as one or the other because the inboard conical region cannot objectively be determined to span 40%. This case evolves nearly identically to the marginally conical case however, the conical feature inboard is smaller in size. For this case, the conical structure forms near the 40% location however, it is difficult to locate the boundary of which this structure ends. Due to the ambiguity in defining the end of the conical structure and start of the arch, a *transitional* vortex may be classified as *conical* or *non-conical* depending on where one would define the end of the conical structure.

Figure 3.5 shows the $R^{3.50}_{1.08}$ and $R^{3.50}_{1.36}$ cases and are non-conical LEVs. The $R^{3.50}_{1.08}$ case has an arch structure that spans approximately 60% of the wing while the conical structure spans only about 25% of the wing. This vortex starts off forming similar to that of the conical cases however, a prominent conical vortex structure inboard does not form as large
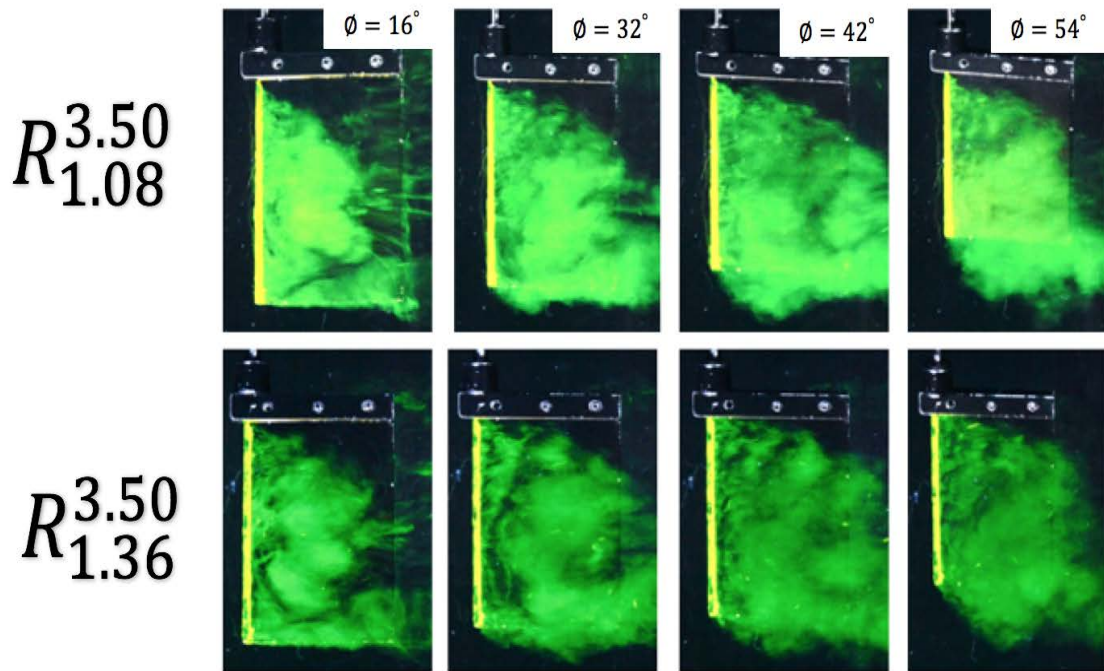
Figure 3.5: Evolution of a *non-conical* LEV

in comparison to the conical case. The arch structure is much closer to the midspan and the overall LEV remains relatively symmetric. A series of LEVs are shed throughout the motion at a relatively high frequency. $R_{1.36}^{3.50}$ shows similar behavior to the case previously discussed with an even smaller conical structure and further exaggerated arch structure. This is the most prominent *non-concial* case.

Using this classification criterion, the LEVs in the parameter space were all classified. The classifications are shown below in figure 3.6

### 3.4    A Rotation Parameter

As observed in figure 3.7 the classification of the LEV behavior across the parameter space has a continuum of behavior which includes a clearly conical region, a clearly
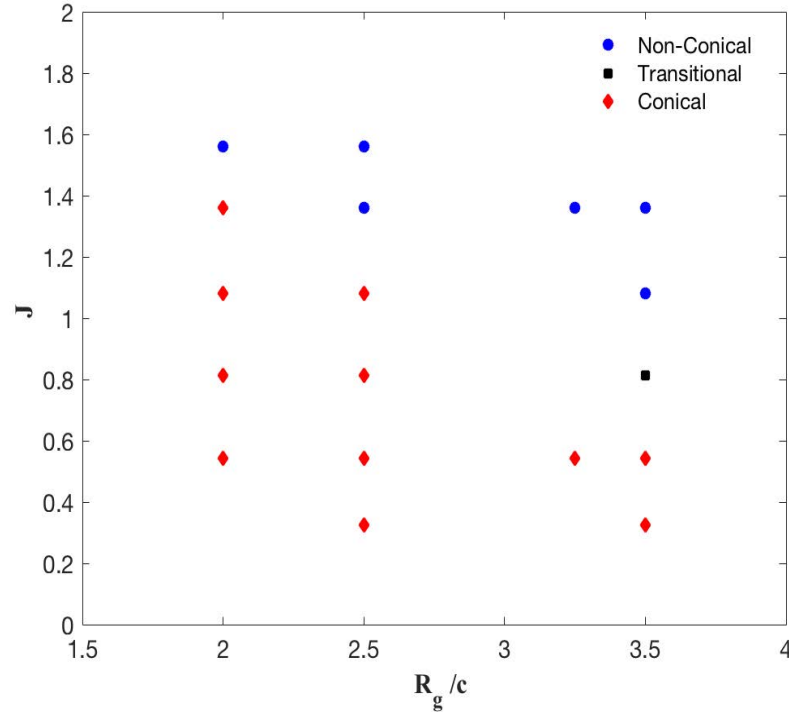
Figure 3.6: LEV classification

non-conical region and a transition threshold which lies in between the two regions. Near

the transition threshold, the LEVs are often difficult to classify as conical or non-conical

because a conical structure forms near the 40% however, the boundary of this structure is

difficult to objectively identify. During the classification of the LEVs across the parameter

space all LEVs were classified as *conical* or *non-conical* with the exception of a single

transitional vortex. There are many candidates that could define the threshold however, a

strong candidate is $\Pi_{Rot}$ parameter. $\Pi_{Rot}$ is a non-dimensional velocity gradient with the

idea that there is a shear approach velocity across the span of the wing:

$$\Pi_{Rot} = \frac{c}{U_{loc}} \frac{\partial U_{loc}}{\partial r} \tag{3.1}$$
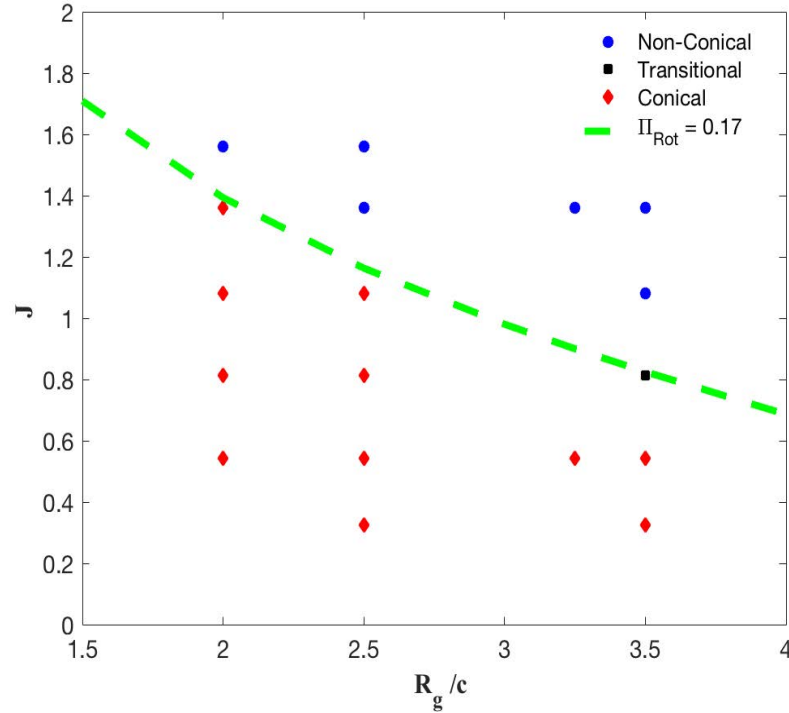
Figure 3.7: $\Pi_{Rot}$ applied to LEV classification

$$U_{loc} = [(\Omega_x r)^2 + (U_\infty)^2]^{\frac{1}{2}} \tag{3.2}$$

where $c$ is the chord, $U_{loc}$ is the local velocity at a given distance away from the radius of gyration, and r is the radial distance away from the axis of rotation. If some mathimatical manipulation of the equation is done to equation 3.1:

$$\Pi_{Rot} = \frac{\Omega_x^2 r}{U_{loc}^2} \tag{3.3}$$

This form of the parameter was derived by Lentik and Dickinson [4] by non-dimensionalizing the non-inertial Navier Stokes equation. This form of the equation how-

ever, is not the most reflective form of the relevant physics analyzed in this study. If further manipulation the equation to equation 3.3:

$$\Pi_{Rot} = \frac{c/R_g}{1 + J^2} \tag{3.4}$$

In this form, the equation is only a function of $J$ and $R_g/c$. When plotted against the LEV classifications, lines of constant $\Pi_{Rot}$ fit very well. Specifically, $\Pi_{Rot} = 0.17$ cuts directly through the conical and non-conical regions and accounts for the transitional vortex.

When the $\Pi_{Rot}$ is above the transition point, the vortex is classified as *non-conical* which corresponds to a $\Pi_{Rot} < 0.17$. A lower $\Pi_{Rot}$ can be achieved either by lengthening the $R_g/c$ or increasing the $J$ value. Increasing the $R_g/c$ reduces the curvature for the path of travel as stated by Lentik and Dickinson [10] which ultimately results in flow similarity to purely translating plates. A similar effect is produced at larger $J$ values as the wing is rotating at a lower rotation rate. The $\Pi_{Rot} < 0.17$ are directly reflected in the physics because often, *non-conical* LEVs are symmetric, 2-D, and produce a large arch structure often observed in purely translating plates.

Below the transitional region, is the conical region which correspond to $\Pi_{Rot} > 0.17$. Too increase increase $\Pi_{Rot}$ above the threshold value, the $J$ or the $R_g/c$ value must be decreased. Decreasing the $J$ value increases the rotation rate which in turn increases the rotational shear and rotational effects on the flow. A decrease in $R_g/c$ results on an increase in rotational effects overall and particularly inboard as stated by Lentik and Dickinson [10]. These results are consistent with the observations of Bross et. al (2015)[2] in which they

found that the LEV structure is relatively insensitive to the $J$ at lower $R_g/c$ because the parameter space was focused in the conical region.

Ultimately, this would suggest that $\Pi_{Rot}$ is the governing parameter in classification of the LEV and accurately accounts for the kinematic as well as the geometric effects that are relevant in determining the structure of the LEV.

### 3.5    Force Measurements

Figure 3.8 shows the lift and drag coefficients for the $R_{1.36}^{3.25}$, $R_{1.36}^{2.50}$, $R_{0.54}^{3.25}$, and $R_{0.54}^{2.50}$ cases. The top and bottom rows of the figure are the force coefficients non-dimensionalized by the free-stream velocity and relative velocity respectively. The definition of the force coefficient non-dimensionalized by $U_\infty$ are shown in equations while the equation show the non-dimensionalization by the relative velocity. Overall, the lift coefficients have more trends than the drag coefficient. For $J = 1.36$ cases (i.e. $R_{1.36}^{3.25}$ and $R_{1.36}^{2.50}$), a high oscillation frequency is apparent and related to the shedding of vortices. The force coefficients for the low advance ratios however, have an inertial peak at the beginning of the motion and is followed by a irregular udulations related to events occurring in the formation and evolution of the LEV.

Unlike the lift coefficients, the drag coefficient magnitudes and behaviors are all different for the 4 cases. For the $R_{1.36}^{3.25}$, the drag is highly oscillatory as observed in the lift coefficient. The magnitudes of the peaks increase as the motion progresses. The $R_{1.36}^{2.50}$, case follows a similar oscillation frequency as the $R_{1.36}^{3.25}$ case however, the drag has far smaller relative magnitude peaks and stays fairly consistent with no significant increase or decrease
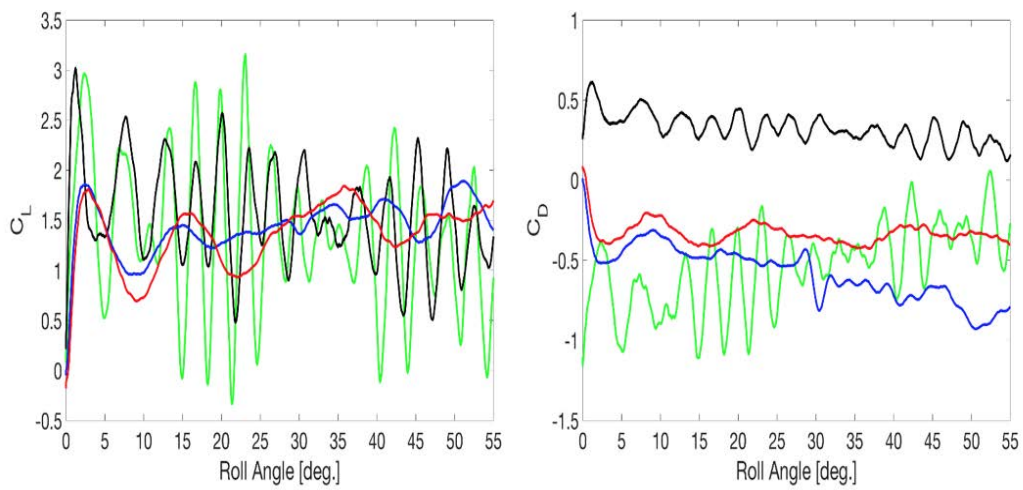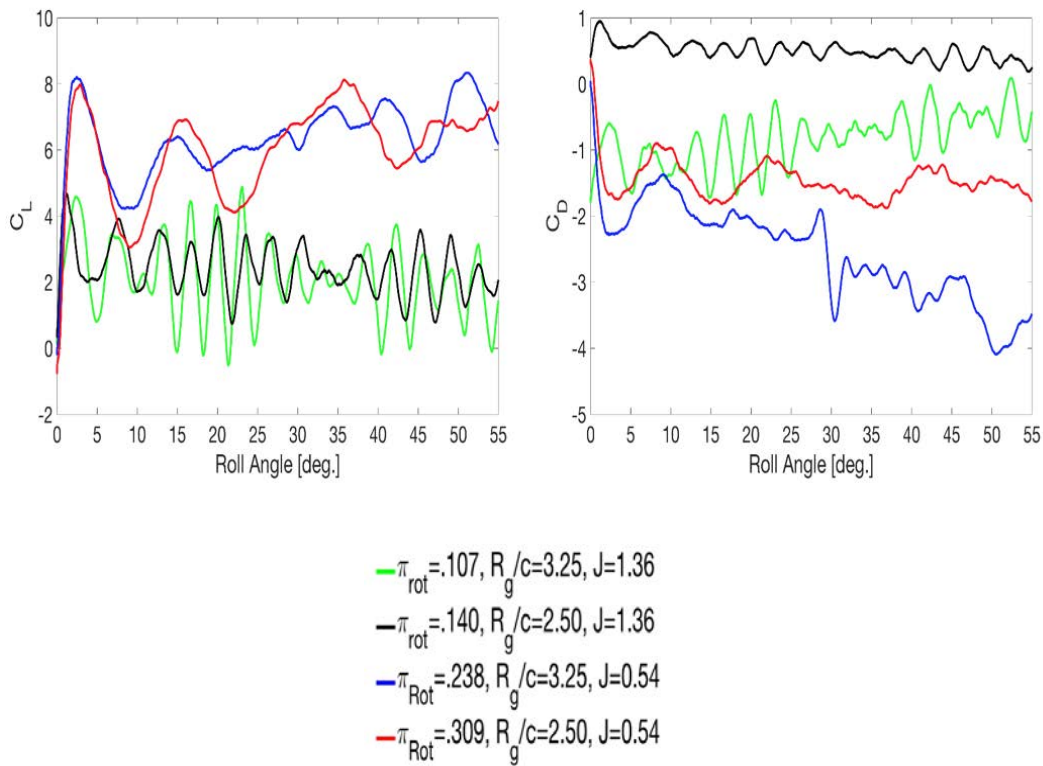
Figure 3.8: Force coefficients scaled by $U_\infty$ (Top) and $U_{rel}$ (Bottom)

in the magnitude of the peak. At the higher rotation rates corresponding to $J = 0.54$, forces do not fluctuate as frequently. For the $R_{0.54}^{3.25}$ case, the forces start with an initial drop in drag which appears to be a transient effect and product of the large initial $\alpha_{geo}$ angle. Following this initial transient the drag forces oscillate at a far lower frequency than that at higher J values. The magnitude of the large peaks stay relatively consistent across the motion. Finally, $R_{0.54}^{2.50}$ follow a similar overall trend as the $R_{0.54}^{3.25}$ case however the magnitude of the low frequency oscillations in force appear to have decreasing magnitudes in thrust as the flow evolves. The $R_{0.54}^{2.50}$ case contrary to other 3 cases produced a net drag instead of thrust.

Fluctuations in the force are related to events that are observed in the flow via the isocontours in figure 3.2 for both $R_{0.54}^{3.25}$ and $R_{1.36}^{3.25}$ cases. In figure 3.8, it can be seen that around $\phi = 17°$ the lift coefficient decreases while the drag coefficient increases. This change in forces coincides with the onset and formation of the arch structure in the outboard region as mentioned in section 2.5. By $\phi = 30°$ another LEV has rolled up which attributes to an increase in lift along with an increase in thrust. At $\phi = 40°$, there is a local maxima in the lift coefficient and a local minima for the drag coefficient. This is related to the shedding of the outboard portion of the initial LEV and the presence of the a dual vortex structure. The dual vortex structure increases suction near the surface of the wing and increases the overall lift as well as reduce the drag. An increase in lift and decrease drag occurs at $\phi = 49°$. This change in the forces is most likely due to the increase in vorticity at the tip of the wing.

For the $R_{1.36}^{3.25}$ case, the forces fluctuates at a very high frequency consistent high shedding frequency for this case. However, the high-frequency oscillations appear to be

contained within a lower "beat frequency" envelope of oscillations. The origin of this beat frequency is not well understood, but may be related to the trailing-edge vortex shedding from a slightly different frequency the leading-edge vortices or, or artifacts of the measurement system.

Noticeably, the relative magnitudes of the force were dependent on if the forces were scaled by the free stream velocity or relative velocity. For the lift coefficient, the $R_{0.54}^{3.25}$ and $R_{1.36}^{2.50}$ cases have higher lift coefficient values when the forces are scaled with $U_\infty$. The $R_{1.36}^{3.25}$ and $R_{1.36}^{2.50}$ cases however produce large scale peak magnitudes when the forces are scaled by the relative velocity. Overall, scaling by the relative velocity decreases the magnitudes of the force coefficient. Scaling by the free stream velocity gives a closer relationship to the raw forces recorded from the data however, scaling by the relative velocity may be a more reflective relationship of the physics occurring at different approach velocity (i.e. different advance ratios or reduced frequencies).

### 3.6   Qualitative Characterization Of LEV Development For Passive Bleeding

Figure 3.9 and 3.10 show the flow evolution of the baseline case and the passive bleeding cases at the smaller and larger hole diameters respectively. All the flow control cases were performed at $J = 0.54$ and $R_g/c = 3.25$. Comparisons are made with the unperturbed case, discussed in the previous section which will be referred to as the baseline case. Figure 3.9 b shows the LEV evolution of passive bleeding with a hole diameter of 1.6 mm at $z/b \approx .1$. By $\phi = 16°$ the LEV has formed across the span of the leading edge and is far more diffuse than the baseline case. Additionally, a tight energetic tip vortex is present

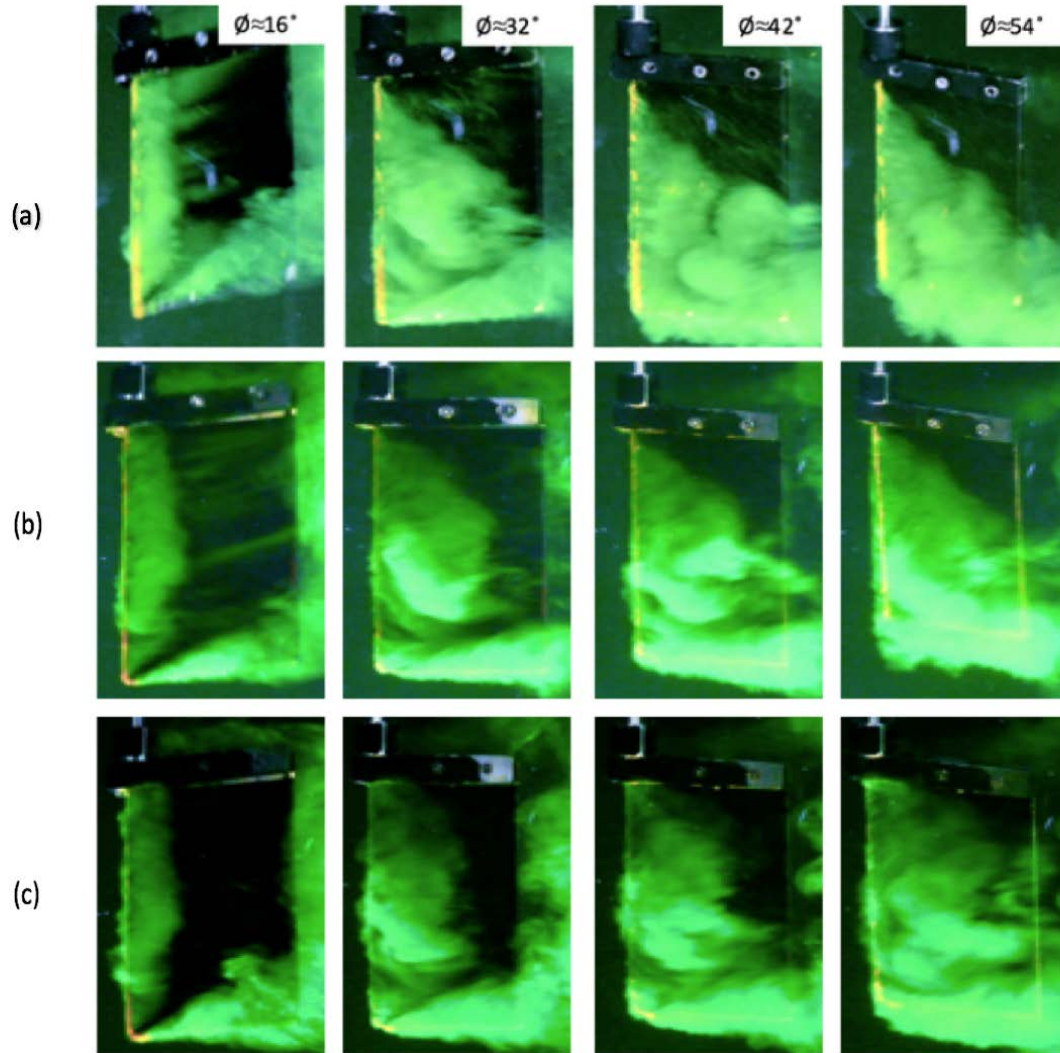Figure 3.9: LEV evolution for $J = 0.54$, $R_g/c = 3.25$, $\alpha_{eff} = 35°$ with (a) absence of Passive Bleeding (b) passive bleeding at $z/b \approx 0.1$, $d = 1.6$ mm ($p_{is}$) (c) passive bleeding at $z/b \approx 0.16$ , $d = 1.6$ mm ($p_{os}$)

in both the baseline and the *pis* case. A conical region forms to about the 40% spanwise location by $\phi = 32°$ similar to that in the baseline case however, the conical LEV is diffuse and not as energetic compared to the baseline case. The rest of the flow evolves similar to that of the baseline which involves the persisting of the inboard conical LEV structure.

Figure 3.9 c is a visualization for a hole of diameter 1.6 mm at $z/b \approx 0.16$. For this case, The flow evolves similar to the case mentioned in the prior paragraph until $\phi = 16°$. The conical inboard region found in the baseline case as well as the previous case does not develop as coherently. A large arch structure forms near the midspan of the wing similar to that of an non-conical LEV absent bleeding however, the flow is far more 3-dimensional. The conical vortex inboard remains however, is still far less coherent than that of the baseline case at $\phi = 42°$. The arch structure near the midspan of the wing is still present however, is not as well defined as any of the previous cases in the absence of passive bleeding. By $\phi = 54°$, the arch structure appears to be the dominant feature in the flow covering about 60% of the wing. The conical structure at the inboard portion of the wing is still present however now only spans to about the 30% location of the wing. The tip vortex appears to have an interaction with the arch structure that has changed its shape.

The LEV of the passive bleeding case with a hole diameter of 3.2 mm and $z/b \approx .1$ shown in figure 3.10 c, evolves much differently than that of the wing in the absence of bleeding. The passive bleeding case starts off with a symmetric LEV that has rolled up by $\phi = 16°$. Similar to the previous bleeding cases, a tip vortex forms however, is only present till $\phi = 32°$. At this point in the motion, a large arch structure forms near the midspan covering approximately 70% of the wing. A conical LEV is not present. By $\phi = 42°$, the
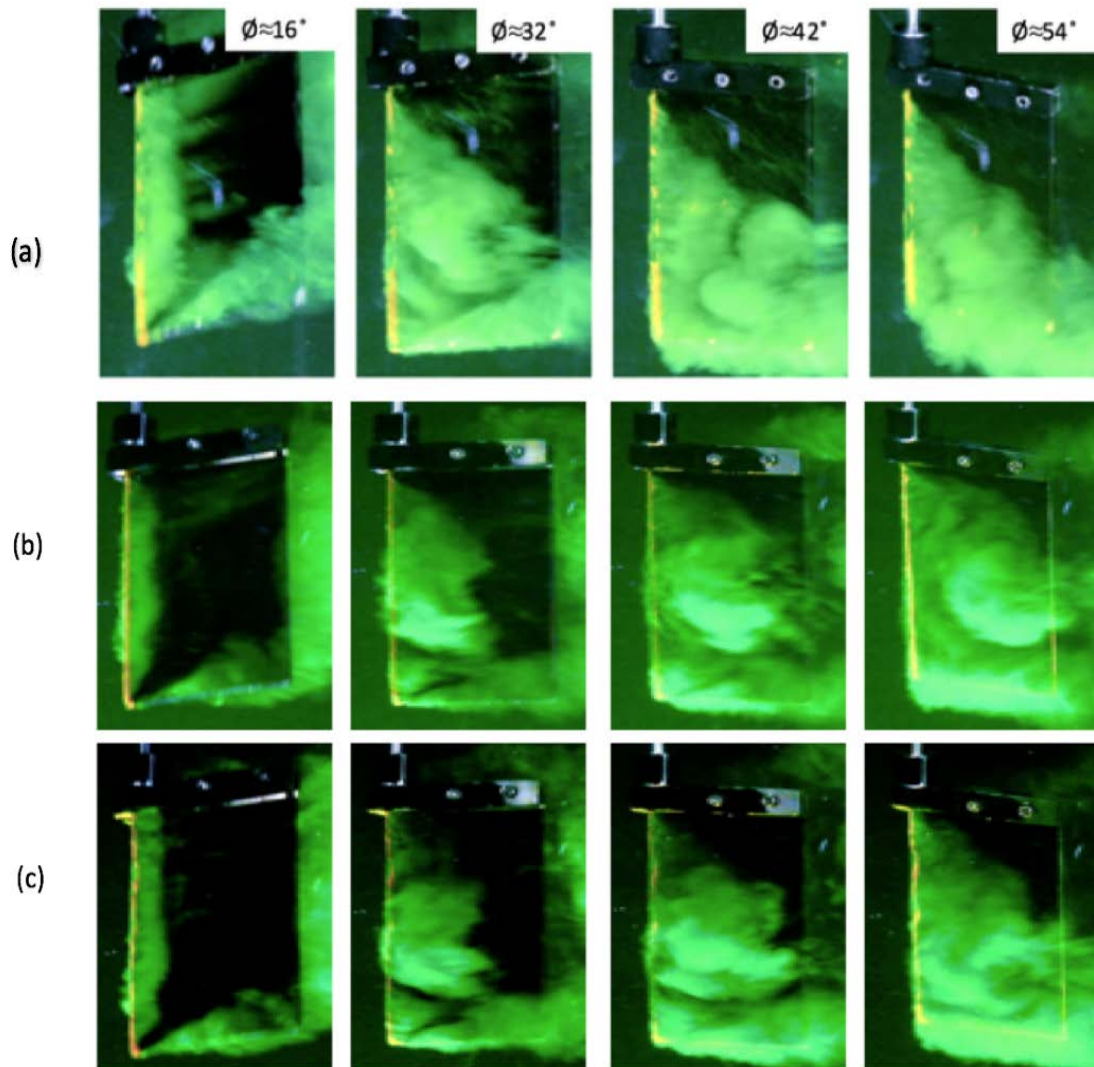
Figure 3.10: LEV evolution for $J = 0.54$, $Rg/c = 3.25$, $\alpha_{eff} = 35°$ with (a) absence of Passive Bleeding (b) passive bleeding at $z/b \approx 0.1$, $d = 1.6$ mm ($p_{is}$) (c) passive bleeding at $z/b \approx 0.16$ , $d = 1.6$ mm ($p_{os}$)

tip vortex has become tube shaped and has begun to interact with the arch structure. This may suggest that the spanwise convection is somehow affected by the passive bleeding. The arch structure sheds by $\phi = 54°$ and the tip vortex is not observed. This case in particular would be classified as a non-conical LEV. This LEV remains symmetric as in the $R_{1.36}^{3.25}$. Another important observation is that even though this passive bleeding case is non-conical, LEV is formed and shed at a much lower frequency than the $R_{1.36}^{3.25}$ case.

The final configuration has a similar evolution to the baseline case however, the conical LEV is not as apparent. One possibility for this is that the magnitude of vorticity is decreased and less dye is entrained. The other possibility is that the dye consistency was different and did not diffuse as effectively between cases.

From all the passive bleeding configurations, configurations $p_{os}$ and $p_{il}$ appear to have the most impact on the flow and reduce the conical inboard region while increasing the large arch structure near the midspan. This is very important in the sense that the flow structure was drastically altered while the kinematics and the geometry was kept the same. This will provide a crucial platform for studying the mechanisms involved in the formation and evolution of the LEV through flux analysis.

The forces of the passive bleeding case in comparison to the baseline $R_{0.54}^{3.25}$ case are plotted in Figure 3.11 to further understand the impact of the flow has on the aerodynamic forces. From a broad perspective the lift coefficient for the is far more predictable than the drag coefficient. The lift coefficients of both the flow control case and the baseline case follow the same characteristic curve which includes an initial transient peak followed by the low frequency oscillations. This is expected when relating the forces to the flow
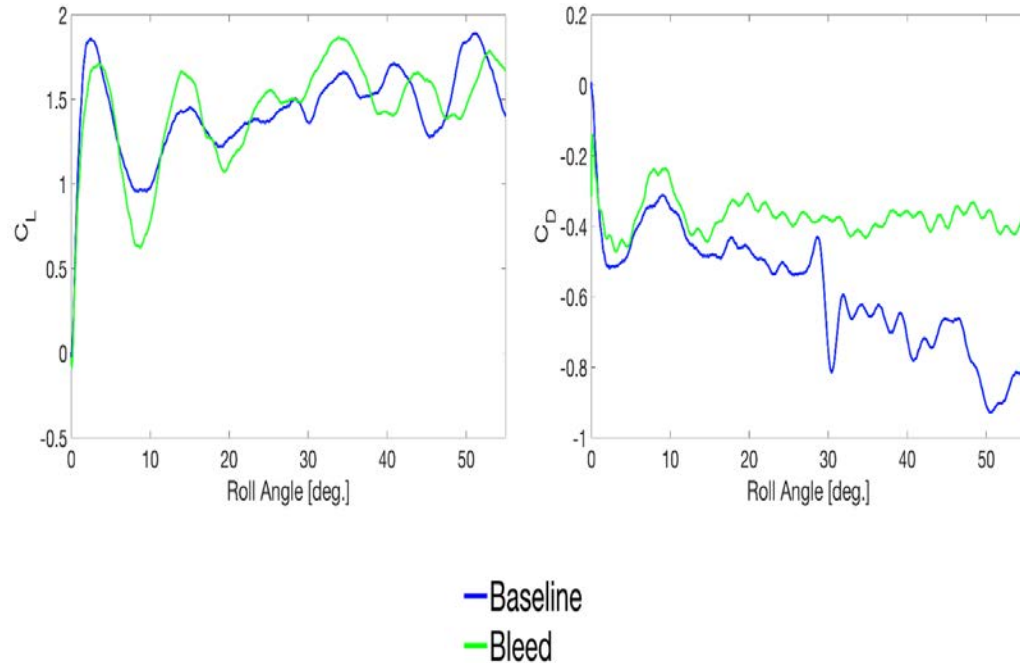
Figure 3.11: Force coefficients for baseline and passive bleeding scaled by $U_{rel}$

visualizations prior. For the passive bleeding case, even though the LEV is classified as a non-conical structure, shedding occurs at a low frequency. This means that we would not expect to see the high frequency fluctuations in force as seen by a non-conical case such the $R^{3.25}_{1.36}$ case. One noticeable difference difference in the forces appears in the drag. After an inertial peak, the baseline case has a steady decrease in magnitude of the peaks however for the passive bleeding case the thrust is reduced due to the shedding of the LEV which produced suction.

# CHAPTER 4
# CONCLUSION/ FUTURE PROJECTS

## 4.1    Conclusion

A broad spectrum of cases were visualized with a focus on varying $J$ and $R_g/c$. Observation of the flow showed that a significant identifying feature was the conical inboard region which appeared during when rotational effects dominated the flow. When the conical inboard region did not form, the flow resembled a purely translating plate and remained fairly symmetric as well as 2D. From these observations, a classification criterion was defined based on *conical* and *non-conical* behavior. A continuum of LEV evolutions were observed between the conical and non-conical LEVs. The *conical* LEVs formed a conical LEV structure inboard that spanned to at least the 40% spanwise location to at least $\phi=$ 40°. Any vortex that does not meet the *conical* LEV criterion is classified as a *non-conical* LEV. Due to the continuum of LEV evolutions across the parameter space, there were also *transitional* vortices. A *transitional* vortex was a vortex that formed a conical LEV structure near the 40% although it is difficult to subjectively identify the boundary of the conical structure so this vortex can be classified as either *conical* or *non-conical* depending where the boundary is determined to be. $\Pi_{Rot}$, a non-dimensional velocity gradient, was proposed to be the governing parameter in determining the initial LEV classification. The $\Pi_{Rot}$ parameter, accounts for both rotational and the geometric effects (i..e. $J$ and $R_g/c$). Lift and drag were then measured to find how the different flow structures impact the forces on the wing. The $R_{0.54}^{3.25}$ and $R_{1.36}^{3.25}$ cases which produced *conical* LEVs, had an inertial peak fol-

lowed by irregular udulations related to events in the flow. The $R_{1.36}^{3.25}$ and the $R_{1.36}^{2.50}$ cases had high frequency oscillations that were related to the high shedding frequency of the LEV along with other artifacts.

Passive bleeding was applied to a baseline case of $R_{0.54}^{3.25}$ with 2 different hole locations and 2 different hole diameters. The baseline case produced a *conical* however, it was found passive bleeding at the most inboard location with the largest hole diameter (i.e. The $P_{il}$ case) perturbed the flow significantly and transformed the LEV to a *non-conical* classification. This was significant because the flow was drastically changed while maintaining the same kinematic and geometric parameters. This will serve as a platform for future analysis via flux analysis in identifying the governing mechanisms for LEV evolution and formation. The forces for this particular passive bleeding case did not have a significant impact on the lift but did reduce drag to nearly 0. This was related to the reduction in the suction that is generally created by the attached LEV conical region inboard on the wing.

## 4.2   Future Work

In this section a summary of work that is currently conducted as well as future projects will be discussed. In the discussion, both the method along with the overall relevance of the project will be identified.

The focus of this paper was to understand $J$ and $R_g/c$ on the overall flow structure of rotating wings in the presence of free stream however, a vorticity transport analysis, in which the sources and sinks of circulation governing LEV growth is useful to identify the mechanisms that governs LEV formation and evolution as well as forces produced by the

wing. A vorticity transport analysis on both rolling wings in the absence as well as with passive bleeding can be used to identify the fundamental changes in transport that occur to yield disparate vortex structures with identical wing kinematics.

Overall the general approach of the research field is to first understand flow of purely pitching, rolling and plunging wings then progress towards increasingly complex kinematics. For future work combinations of these kinematics will be studied as wing maneuvers as well as other applications such as flapping flight are generally not singular motions. Currently, pitching introduced in a roll environment is being studied from a topological stand point as well as a vorticity transport perspective using plenoptic PIV data that was captured. Given that the addition of pitch introduces a new variable, the pitch rate $\dot{\alpha}$, the relevance of the $Pi_{Rot}$ to the pitch/roll case needs to further be investigated.

In past work, one proposal was that the secondary vorticity near the surface of a rolling wing is the mechanism that keeps the LEV attached. This hypothesis was briefly tested by Akkala et. al [1] for a purely plunging wing however no conclusions were drawn. For future work, perturbing the flow with forced methods can help support or weaken the argument that secondary vorticity is the mechanism controls LEV attachment. Additionally,time-dependent mechanism can also be tested by using forced perturbations at different points of the motion. In the past preliminary flow visualizations were done using tubing and a syringe to identify impact on the flow. This effort showed no significant results however, the forced perturbations were controlled and could not be applied at desired points in the motion.

# REFERENCES

[1] James Akkala. *Flow structure and performance of a flexible plunging airfoil*. PhD thesis, University of Iowa, 2013.

[2] M. Bross, C.A. Ozen, and D. Rockwell. Flow structure on a rotating wing: Effect of steady incident flow. *Phys. Fluids*, 25:081901, 2013.

[3] C. P. Ellington, C. van den Berg, A. P. Willmott, and A. L. R. Thomas. Leading-edge vortices in insect flight. *Nature*, 384:626–630, 1996.

[4] D. f and M. H. Dickinson. Biofluiddynamic scaling of flapping, spinning, and translating fins and wings. *J. Exp. Biol.*, 212:2691–2704, 2009.

[5] Timothy W Fahringer, Kyle P Lynch, and Brian S Thurow. Volumetric particle image velocimetry with a single plenoptic camera. *Measurement Science and Technology*, 26(11):1–25, 2015.

[6] H. Himmelskamp. *Profile Investigations on a Rotating Airscrew*. PhD thesis, Göttingen, 1945.

[7] T. Jardin and L. David. Spanwise gradients in flow speed help stabilize leading-edge vortices on revolving wings. *Phys. Rev. E*, 90:013011, Jul 2014.

[8] Kyle C Johnson, Brian S Thurow, Taehoon Kim, Gianluca Blois, and Kenneth T Christiansen. Volumetric velocity measurements in the wake of a hemispherical roughness element. *AIAA Journal*, July:1–16, 2017.

[9] A. R. Jones and H. Babinsky. Unsteady lift generation on rotating wings at low reynolds numbers. *J. Aircraft*, 47(3):1013–1021, 2010.

[10] D. Lentink and M. H. Dickinson. Rotational accelerations stabilize leading edge vortices on revolving fly wings. *J. Exp. Biol.*, 212:2705–2719, 2009.

[11] M. A. Mendez, M. Raiola, A. Masullo, S. Discetti, A. Ianiro, R. Theunissen, and J. M. Buchlin. POD-based background removal for particle image velocimetry. *Experimental Thermal and Fluid Science*, 80:181–192, 2017.

[12] M. Visbal, T. O. Yilmaz, and D. Rockwell. Three-dimensional vortex formation on a heaving low-aspect-ratio wing: Computations and experiments. *JFS*, 38:58–76, January 2013.

[13] C. J. Wojcik and J. H. J. Buchholz. Parameter variation and the leading-edge vortex of a rotating flat plate. *AIAA J.*, 52(2):348–357, 2014.

[14] M. Wolfinger and D. Rockwell. Flow structure on a rotating wing: effect of radius of gyration. *Journal of Fluid Mechanics*, 755:83?110, 2014.

[15] Maxwell Wolfinger and Donald Rockwell. Transformation of flow structure on a rotating wing due to variation of radius of gyration. *Experiments in Fluids*, 56(7):137, Jun 2015.

[16] J. Zhou, R. J. Adrian, S. Balachandar, and T. M. Kendall. Mechanisms for generating coherent packets of hairpin vortices in channel flow. *J. Fluid Mech.*, 387:353–396, 1999.